

Hot electrons and dark excitons modulate exciton-photon strong coupling in metal-organic optical microcavities

Pavel V. Kolesnichenko,^{*,†,‡} Manuel Hertzog,[†] Felix Hainer,^{†,‡} Oskar Kefer,^{†,‡}

Jana Zaumseil,[†] and Tiago Buckup^{*,†,‡}

[†]*Physikalisch-Chemisches Institut, Ruprecht-Karls-Universität Heidelberg, 69120,
Heidelberg, Germany*

[‡]*Institute for Molecular Systems, Engineering and Advanced Materials,
Ruprecht-Karls-Universität Heidelberg, 69120, Heidelberg, Germany*

E-mail: pavel.kolesnichenko@alumni.uni-heidelberg.de; tiago.buckup@pci.uni-heidelberg.de

Abstract

Polaritons are promising for important applications including organic solar cells, optical logic gates, and qubits. In low-Q microcavities, polaritonic signatures of strongly hybridized photons and Frenkel excitons were previously found to decay together with dark excitons. There remain unresolved questions regarding whether dark excitons affect the strength of exciton-photon coupling. Additionally, the contributions of dark excitons in organic layers and hot electrons in metal films to the polaritonic response are not fully understood. Here, we identified that due to delocalization of polaritons over organic and metal layers, they are sensitive to both dark excitons and hot electrons. Dark excitons modulate exciton-photon coupling strength, whereas hot-electrons imprint two-temperature dynamics onto the polaritonic response. Both organic and metal films contribute to transient Fano-like gain-loss spectra of exciton-polaritons. These and other mechanistic insights into the strong-coupling dynamics were supported by the theory of non-Hermitian Hamiltonian mechanics, axially-resolved optical simulations, global analysis of pump-probe spectra, and statistical correlation analysis. The developed methodology can be applied to other microcavity structures. Our findings are important for disentangling pure polaritonic effects from other excitations in organic and metal layers, with the ultimate aim of achieving photonic control over photophysical and photochemical processes.

Keywords

microcavity, photonics, polaritons, excitons, hot electrons

Introduction

Exciton-polaritons are hybrid quasi-particles which are formed as a result of strong light-matter interactions and inherit properties of both matter and light. They are promising for

numerous applications such as terahertz sources and detectors,¹ low-threshold lasers,² all-optical transistors,³ refractive index sensors,⁴ organic solar cells,⁵ spatial light modulators,⁶ and qubits.⁷ On a more fundamental side, they have been used in studies of Bose-Einstein condensates,⁸ superfluids,⁹ and acoustic black holes,¹⁰ only to mention a few.

Strong coupling of light to matter and related phenomena have been commonly studied with Wannier-Mott excitons in the active (semiconductor) layer of optical microcavities. More recently, organic matter has gained popularity because it can provide large density of Frenkel excitons with large binding energies allowing investigations of polaritonic phenomena even with low-Q microcavities and at room temperature.^{11–17} This has allowed the observation of such polariton-enhanced phenomena as, for example, superabsorption for energy storage,¹⁸ enhanced photoluminescence for lasing applications,¹⁹ and, for optoelectronic applications, enhanced energy-transfer through heterojunctions,²⁰ enhanced singlet fission (SF)²¹ and μ s-long polariton lifetime.²² The scenarios of polariton-assisted enhancement of useful effects, however, may not always occur.^{21,23–25} Thus, for example, strong coupling of surface plasmons to chromophores may not result in mesoscale energy transfer.²³ In the case of SF, the exciton fission efficiency can decrease either through the photonic leakage of polaritonic states,²¹ or, when mediated by conical intersection, due to poorer Franck-Condon overlap emerging in the hybrid system.²⁵

Recent time-resolved experiments aiming at revealing the effects of strong coupling on SF in low-Q organic microcavities also showed no enhancement of triplet formation yield.²⁴ At the same time, strong dispersive signatures of exciton-polaritons lasted as long as the lifetime of dark triplet excitons. This has been explained by the very fast decay of polaritons to the manifold of long-lived dark states before any photonic leakage occurred.^{24,26} The observed polaritonic response was attributed to changes in the number of coupled molecules and the effective refractive index of the cavity.²⁴ Even when perturbing optical properties of the metal layers alone (with no dark excitons involved) using infrared photons, it was still possible to observe polaritonic signatures near the main exciton resonance in the visible.²⁷ In

these experiments, the observed signals represented rather strong-coupling conditions than long-lived polaritons¹⁶ since there was no pump-induced population of polaritonic states. In this case, however, Rabi energy quantifying strong coupling was not observed to be sensitive to changing photonic environment of the cavity, which remained to be established. These case-studies, nevertheless, suggest that the strong optical response at the energies of hybrid modes can contain information on carrier dynamics in both active and metal layers. Their disentanglement, however, remained a challenge as well as their manifestation in the nonlinear optical response unclear.

Here, we disentangle the main contributions to the optical transient response of a low-Q all-metal optical microcavity (using TIPS-PEN in the active layer) under strong coupling conditions. We combine time-resolved spectroscopy over four orders of magnitude in time with a theoretical modelling and analysis. Polaritons were found to be delocalized over both organic and metal layers inheriting information on the dynamics of dark excitons and hot electrons, respectively, modulating photonic environment and strong coupling. First, strong coupling is quantified through the Rabi energy that is demonstrated to be strongly correlated with the dynamics of dark excitons undergoing SF in the organic layer. Next, dark excitons are shown to contribute additional phase offsets to polaritonic resonances responsible for changes of the Rabi energy. In addition, metal films are found to contribute absorptive components near the energies of polaritonic branches further shaping nonlinear optical response. Finally, contributions from hot electrons were unambiguously identified via statistical correlation analysis of time-constants from a large pump-probe dataset. Overall, the joint response of the organic and metal layers leads to Fano-like optical gain-loss spectrum at polariton energies. These findings are additionally supported by the analysis based on non-Hermitian Hamiltonian mechanics and *ab initio* transfer-matrix (TM) simulations.

Results

Strong coupling and polariton delocalization

Angle-resolved steady-state reflectance spectra of polaritons in two cavities of different thicknesses are shown in Fig. 1a,b, with hybridized modes indicated (see Supplementary material, Section S1, for further details). These modes reflect strong coupling of excitons and photons giving rise to quasi-particles with intermediate effective masses (band curvatures) referred to as exciton-polaritons or, simply, polaritons. The two lowest-energy polaritons are referred to as upper (UP) and lower (LP) polaritons. Since bare excitonic bands (X_α and X_β) are not discernible, they are referred here to as the bands of dark excitons, *i.e.*, excitons that have not coupled strongly to the cavity mode C . The UP-LP splitting magnitude at the bands' minima for the thin cavity (Fig. 1a) is ~ 110 meV, whereas that for the thick cavity (Fig. 1b) is ~ 100 meV. This difference in the interband polaritonic splitting is a consequence of different detunings of the cavity mode from the main excitonic resonance (Fig. 1a,b). Coupling strength at a given angle is characterized by the Rabi energy, which generally coincides with the interband polariton splitting in the regions where cavity mode crosses excitonic resonance. Such crossing between C and X_α never occurs in thin cavity (Fig. 1a), contributing to a larger energy separation between UP and LP. There is a third polaritonic band present at ~ 2.1 eV, which is mostly excitonic in nature, and therefore not explicitly considered here.

More formally, the two significant polaritonic branches (UP, $|\psi_+\rangle$, and LP, $|\psi_-\rangle$) are the result of hybridization of uncoupled states of exciton ($|\psi_{X_\alpha}\rangle$ and $|\psi_{X_\beta}\rangle$) and photon ($|\psi_C\rangle$),

$$|\psi_\pm\rangle = \sqrt{\alpha_\pm}|\psi_{X_\alpha}\rangle + \sqrt{\beta_\pm}|\psi_{X_\beta}\rangle + \sqrt{\gamma_\pm}|\psi_C\rangle, \quad (1)$$

where, $\alpha_\pm, \beta_\pm, \gamma_\pm$ are Hopfield coefficients defining curvatures of polaritonic bands (Fig. 1a,b) through how much there is excitonic (α_\pm, β_\pm) and photonic (γ_\pm) contribution to each of them. Thus, in the case of thin cavity (Fig. 1a), UP inherits larger photonic fraction compared to

LP, whereas, in the case of thick cavity it is the LP band that is more photonic in nature than UP (see Supplementary material, Section S2, for estimations of Hopfield coefficients, and Table 1 for excitonic and photonic contributions to UP and LP). In Eq. (1), other, less intense, vibronic states that also participate in hybridization are omitted due to their negligible contribution.

The band with a greater degree of photonic nature results in a larger absorption strength (Fig. 1d) due to the cavity-facilitated local field enhancement effects²⁸ (see Supplementary material, Section S3, for local field simulations), similarly to what was observed previously for amorphous rubrene.²⁹ The larger photonic field of a more photonic polariton also yields a stronger absorption at similar energies in metal layers within their penetration depth. This renders polaritons to be not only delocalized over the organic layer but also extended into the metal films (as shown in Fig. 1c) making them potentially susceptible to the dynamics of both dark excitons and hot electrons.

Table 1: Excitonic ($\alpha + \beta$) and photonic (γ) contributions to UP and LP of thin and thick cavities, estimated from Hopfield coefficients averaged across the angles from -5° to 5° (see Supplementary material, Section S2).

| | $\alpha + \beta$ | γ |
|------------------|------------------|----------|
| Thin cavity: UP | 46% | 54% |
| LP | 71% | 29% |
| Thick cavity: UP | 69% | 31% |
| LP | 38% | 62% |

Pump-induced dynamics of strong-coupling conditions

To gain insights into exciton-photon coupling dynamics, transient reflectance (TR) experiments were carried out (Fig. 1c). Pump and probe beams were at nearly-normal-incidence angles so that it is the regions close to the bands' extrema in Fig. 1a,b that were predominantly probed. The pump spectrum was tuned to overlap with the energy of X_α -resonance of uncoupled excitons (Fig. 1d), thus, in addition to polaritons and hot electrons, exciting the dark-states reservoir. Differential reflectance (DR) spectra of both samples (Fig. 1e,f,

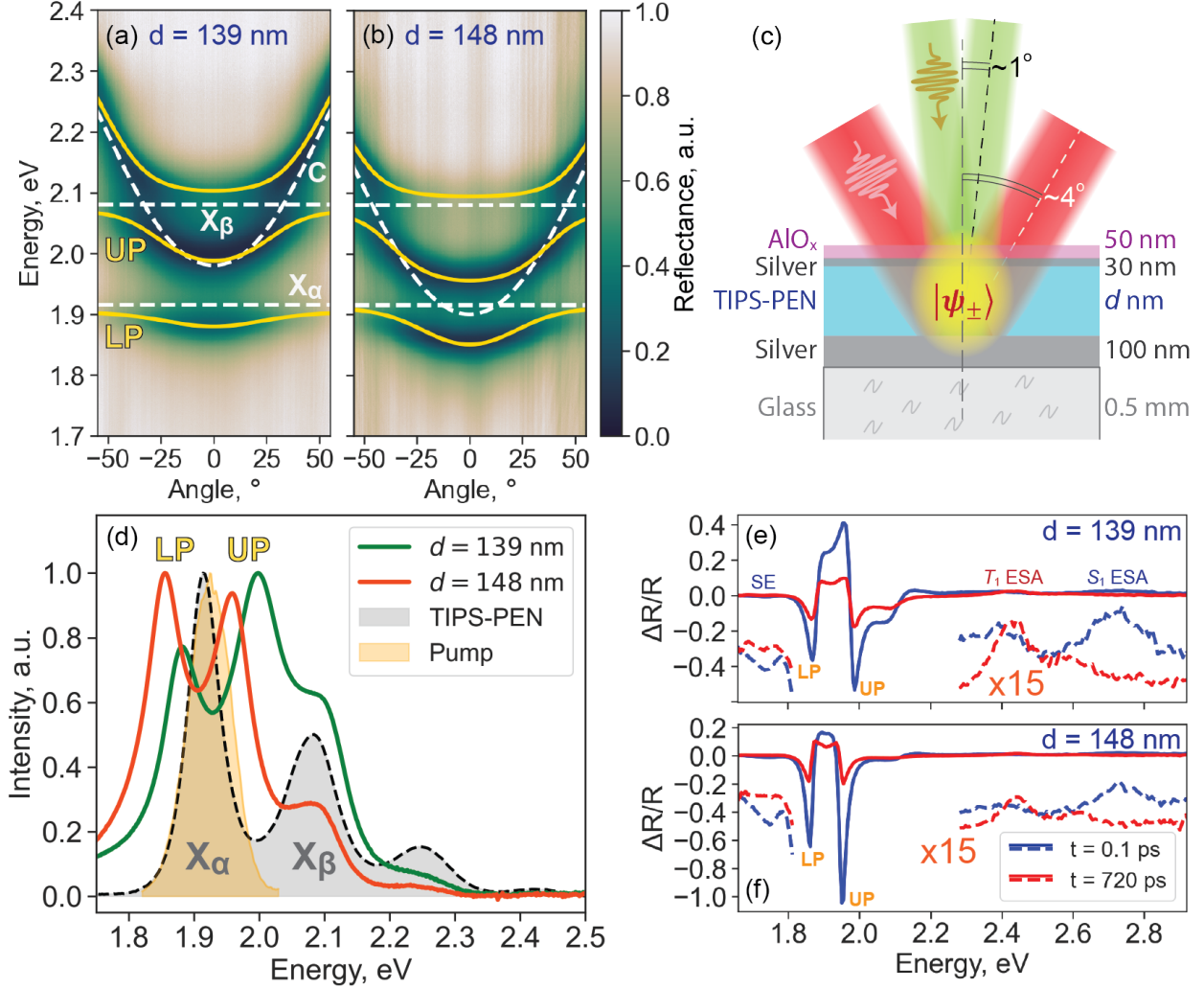


Figure 1: Steady-state and transient spectra of microcavities. (a,b) Normalized angle-resolved steady-state reflectance spectra of (a) thin cavity ($d = 139$ nm) and (b) thick cavity ($d = 148$ nm), with the upper and lower polaritons (UP and LP), dark excitons (X_α and X_β), and cavity mode (C) indicated. Dashed lines represent uncoupled excitonic (horizontal lines) and photonic (parabola) states; solid yellow lines represent hybridized uncoupled (polaritonic) states. (c) Schematics of the transient reflectance experiment. (d) Steady-state absorption spectra of thin (green) and thick (red) cavity, bare TIPS-PEN (dashed and shaded in grey), and pump spectrum (shaded in yellow). (e,f) Transient reflectance spectra at short (0.1 ps, blue) and long (720 ps, red) pump-probe delays of (e) thin and (f) thick cavity. The weak molecular response (dashed) is scaled by a factor of 15 and vertically offset for clarity.

and Supplementary material, Section S4) feature a long-lasting strong dispersive response at the energies of polaritonic bands, which has also been observed previously.^{13,24,27,30} It greatly dominates over the weak molecular response formed from stimulated emission (SE)

in the lower-energy region ($\sim 1.7\text{--}1.8$ eV) and S_1/T_1 excited-state absorption (ESA) in the higher-energy region ($\sim 2.4\text{--}2.8$ eV). The latter corresponds to optical messengers of SF in TIPS-PEN.²⁸ One of the striking differences between thin and thick cavities is the amplitude of the loss (negative) signal at UP and LP energies at early pump-probe delays (< 10 ps). At longer pump-probe delays (> 10 ps), these dramatic differences between the two samples vanish.

We note that the lifetime of such response greatly exceeds expected lifetimes of both UP and LP. Indeed, the estimated cavity-mode lifetime in this study is $\tau_C \sim 9$ fs (cavities' Q-factor is ~ 45), so that polaritons' decay rate $\tau_{\pm}^{-1} = (\alpha_{\pm} + \beta_{\pm})\tau_X^{-1} + \gamma_{\pm}\tau_C^{-1} \gtrsim 30^{-1} \text{ fs}^{-1}$ falls far below the time-resolution of our experiments (~ 100 fs). Therefore polaritons are formed predominantly within the duration of pump and probe pulses and decay into the dark-states manifold within ~ 30 fs following ever-vanishing pulse tails. The pump pulses therefore effectively generate long-lived excitons in the organic layer and hot electrons in metal films; the probe pulses generate short-lived polaritons again, and it is these probe-induced polaritons that experience changing strong coupling conditions (due to excitations in the organic and metal layers). Reflectance difference between pump-perturbed (R_{ON}) and unperturbed (R_{OFF}) cavities results in dispersive gain-loss spectra.

Preliminary spectral analysis of the transient response using singular value decomposition (SVD, see Supplementary material, Section S5) and Fano formulae^{31–33} (see Supplementary material, Section S6) indicated that the spectra are inseparable in time and energy, so that an entangled spectro-temporal model taking into account interference effects is necessary to describe strong coupling. Fano-based description additionally indicated the presence of a weak signal from dark excitons at ~ 1.92 eV overshadowed by the detected strong response at polaritonic energies. Altogether, the evolution of the extracted parameters resembled the course of SF known to occur in TIPS-PEN suggesting that it is at least the dynamics of singlet and triplet excitons that modulated the polaritonic response simultaneously in energy and time.

Notably, similar Fano-like lineshapes have been observed in various other systems where interference of either electromagnetic waves or probabilistic wavefunctions occurred.^{34–42} Most relevant to this work are induced transmission filters (ITFs),⁴² where a strong dispersive DR response resulted from coupling of a 30-nm silver film to a Lorentz-like oscillator, revealing intrinsic strong nonlinearities in the metal layer. Such nonlinear effects of semi-transparent silver films could also contribute to the measured overwhelming nonlinear response in this work. The extracted time-varying Fano-parameters in this case would reflect net dynamics arising from contributions from both organic and metal layers.

Fano formulae describe interband splitting of hybridized bands but not the Rabi energy. Therefore, a non-Hermitian formalism is developed next taking into account interference in the differential-reflectance domain, thus describing entangled spectro-temporal behaviour of the strong polaritonic response.

Singlet-fission dark excitons modulate strong coupling

A strongly-coupled exciton-photon system can be described by the following effective non-Hermitian Hamiltonian:

$$\mathbf{H} = \mathbf{E} + \mathbf{V} + \mathbf{\Gamma}, \quad (2)$$

$$\mathbf{E} = \begin{pmatrix} E_X & 0 \\ 0 & E_C \end{pmatrix}, \mathbf{V} = \begin{pmatrix} 0 & V \\ V^* & 0 \end{pmatrix}, \mathbf{\Gamma} = -\frac{i}{2} \begin{pmatrix} \Gamma_X & 0 \\ 0 & \Gamma_C \end{pmatrix}, \quad (3)$$

where \mathbf{E} contains the energies of exciton (E_X) and photon (E_C); \mathbf{V} describes coupling between them ($V = \hbar\Omega$ is the coupling strength, Ω is the Rabi frequency); and $\mathbf{\Gamma}$ describes spectral widths of exciton (Γ_X) and photon (Γ_C). The eigenvectors of the unperturbed Hamiltonian \mathbf{E} are uncoupled states of exciton ($|\psi_X\rangle$) and photon ($|\psi_C\rangle$). Diagonalization of the Hamiltonian \mathbf{H} (Eq. (2)) yields steady-state eigenfunctions $|\psi_{\pm}\rangle$ and associated eigenenergies $\mathcal{E}_{\pm} = E_{\pm} - i\Gamma_{\pm}$ of the two hybrid oscillators, where E_{\pm} and Γ_{\pm} are their energies and widths, respectively. We note that although there are two vibronic resonances, X_{α} and X_{β} ,

contributing to polaritonic bands in our samples, they could be regarded as one effective exciton, which greatly simplifies analysis yet still allows for main trends to be extracted (see Supplementary material, Section S7, for more details).

Since the measured dispersive lineshapes can be described with Fano formulae almost ideally (as noted above and shown in Supplementary material, Section S6), these lineshapes can be thought of as a result of interference of some kind. Therefore, two phase factors ϕ_{\pm} must enter the description of the two hybrid modes. Since we are interested in the changes of the parameters relative to the initial state (initiated by the pump pulse), we represent the state at any time instance after the pump excitation as a superposition of eigenfunctions of the Hamiltonian \mathbf{H} (Eq. (2)), *i.e.*,

$$|\psi\rangle = e^{i\phi_-} \cos \theta |\psi_-\rangle + e^{i\phi_+} \sin \theta |\psi_+\rangle, \quad (4)$$

where θ controls weights of contributions from each of the polaritonic states, and ϕ_{\pm} were introduced to add relative phase offsets to the two states with respect to the global reference phase $\phi_0 = 0$ defined by the coupling elements in \mathbf{V} . Then, following the Green-function-based approach,^{43–46} transient reflectance can be expressed as

$$\frac{\Delta R}{R} = -\frac{A}{\pi} \Im(G(E)), \text{ with } G = \frac{f_-}{E - \mathcal{E}_-} + \frac{f_+}{E - \mathcal{E}_+}, \quad (5)$$

where f_{\pm} are generalized differential oscillator strengths of the two polaritonic branches defined through *c*-products between the initial and final states,

$$f_{\pm} = (\psi|\psi_{\pm})(\psi_{\pm}|\psi); \quad (6)$$

and A is the scaling factor. We emphasize that since *c*-products (Eq. (6)) are used within the non-Hermitian framework, the phase factors of the polaritonic state-vectors enter the expressions for the oscillator strengths, and therefore nontrivial Fano-like resonances naturally

appear within the framework.

We note that, due to the non-Hermitian nature of the Hamiltonian (Eq. (2,3)), a possibility for being close to exceptional points (*i.e.*, the points where eigenvalues and eigenvectors coalesce) arises.³³ These singularities, or defects, were previously shown to lead to various exotic phenomena^{47–51} including exceptionally long lifetimes,^{52,53} which could potentially explain long polariton lifetimes observed here. We, however, rule this possibility out by simply estimating the distances between UP/LP eigenvalues and eigenvectors which remain far from zero for all pump-probe delays (see Supplementary material, Section S8, for the dynamics of eigenvalues and eigenvectors).

Fig. 2a illustrates intuition behind phases ϕ_{\pm} , which for this sake are remapped onto $\tilde{\phi}_{\pm} = (90^{\circ} + 2\phi_{\pm}) \bmod 180^{\circ}$. The values of $\tilde{\phi}_{\pm}$ simply indicate the peak position of the reflectance spectrum R_{ON} relative to R_{OFF} in the intensity-energy domain. Thus, $\tilde{\phi}_{\pm} = 90^{\circ}$ (-90°) correspond to the loss (gain) signal indicating that R_{ON} spectrum is overall above (below) R_{OFF} spectrum. The values of $\tilde{\phi}_{\pm} = 0^{\circ}, 180^{\circ}$ correspond to more intense purely dispersive lineshapes. Other values describe dispersive profiles with either loss or gain component dominating. The R_{ON} and R_{OFF} peaks slide along the phase-ellipse around their average location. The shape of the ellipse is ultimately fixed by optical density of organic layer, pump fluence, and other experimental conditions; its precise quantification falls beyond the scope of this work. We note that this qualitative picture is fully consistent with general cyclic correlation between temporal phase ($\delta\phi$) and energy (δE) shifts, $\delta E \sim \cos \delta\phi$, for two classical harmonic oscillators,⁵⁴ and that such phase is mappable on the Fano parameter describing gain-loss spectra.⁵⁵ Within the developed framework, the coupling strength V reflects only the average value between "pump-OFF" and "pump-ON" conditions. R_{OFF} spectrum, however, is time-independent, and therefore the dynamics of the Rabi energy V reflects the pump-induced dynamics encoded in the R_{ON} spectrum alone.

The fitting of the polaritonic response with the described model at short (0.1 ps) and long (720 ps) pump-probe delays is of remarkable quality (Fig. 2b), provided the model's

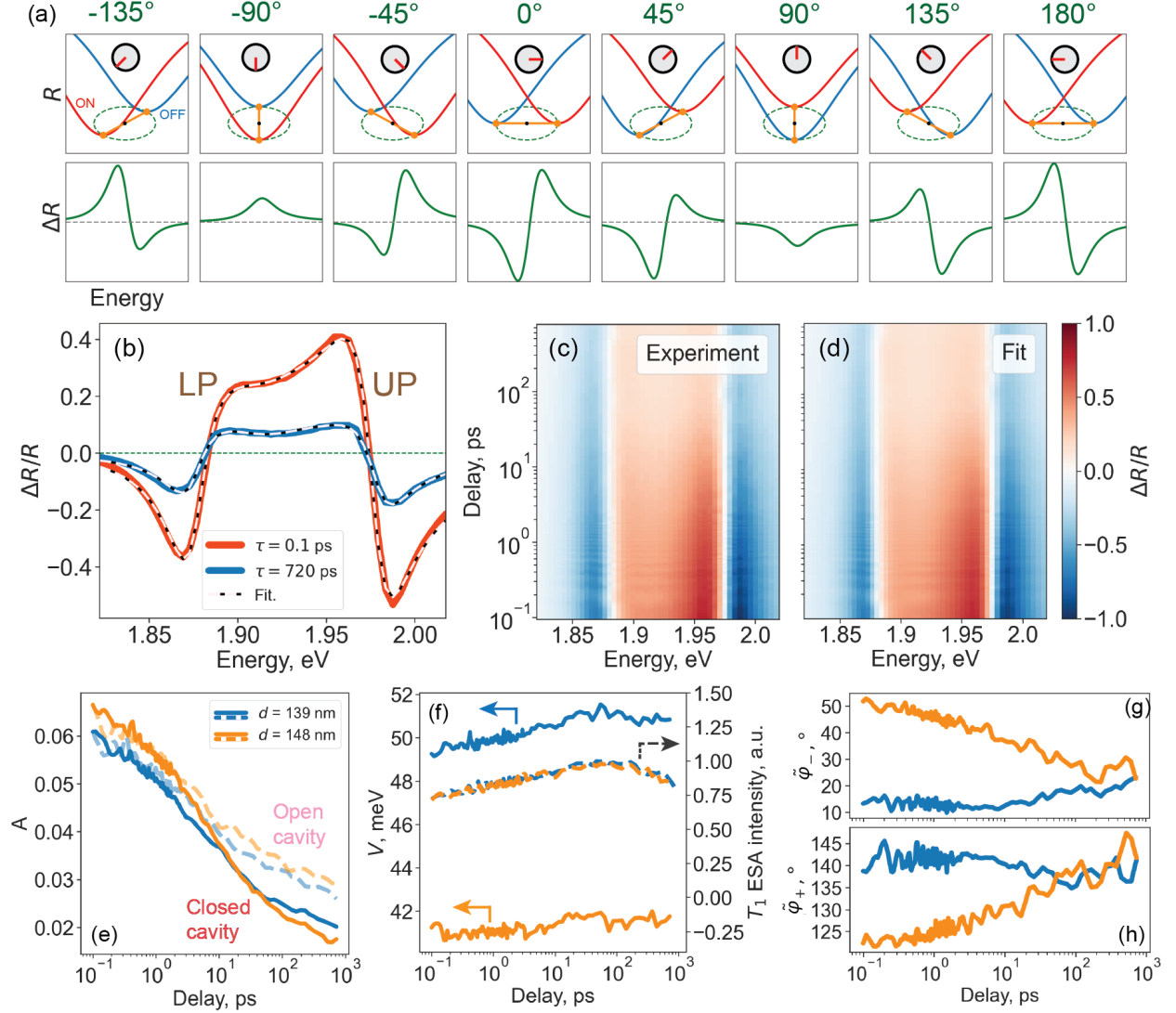


Figure 2: Non-Hermitian Hamiltonian description of transient reflectance spectra. (a) A cartoon explaining the physical meaning of the dynamic phases ϕ_{\pm} after remapping them onto more intuitive values $\tilde{\phi}_{\pm} = 90^{\circ} + 2\phi_{\pm}$ (modulo 180°). (upper row) "Pump-ON" (red) and "pump-OFF" (blue) reflectance spectra. The inset shows the phase $\tilde{\phi}$ and the direction of the offset of the "pump-ON" spectrum relative to the "pump-OFF" spectrum. (b) Fittings (dashed lines) of short- (red) and long-delay (blue) spectra (solid lines) for thin cavity. (c,d) Raw $\Delta R/R$ spectrum (c) and its corresponding fit (d) for thin cavity. (e-h) The scaling amplitude A (e, solid), coupling strengths V (f, solid), and phases $\tilde{\phi}_{\pm}$ (g,h) retrieved from fittings. In (e) dashed lines represent the absolute value of the bleach signal from the corresponding open cavities (*i.e.*, cavities without 30-nm metal film). In (f) dashed lines represent T_1 ESA signal from thin and thick cavities.

simplicity. Comparison of experimental and fitted TR maps demonstrates high fitting quality for all pump-probe delays (Fig. 2c,d). Since a minimum of eight parameters are needed to

describe doubly-dispersive lineshapes (*e.g.*, energy, width, amplitude, and phase per spectral line), overfitting is not the case here: there are precisely eight fitting parameters in our model (excluding a global scaling factor A). An additional parameter describing the intensity of weak uncoupled excitons was, nevertheless, added, enhancing the accuracy of the model in the spectral region around 1.92 eV (see Supplementary material, Sections S9,10, for more details). Global exponential fitting of the extracted parameters revealed that the dynamics is characterized by four time constants similar to exciton dynamics in bare film and open optical microcavities^{24,28} (*i.e.*, cavities without 30-nm metal film) (see Supplementary material, Section S11, for more details).

Fig. 2e–h show evolution of important parameters describing decay of polaritonic response (Fig. 2e), coupling strength (Fig. 2f), and phases (Fig. 2g,h) (see Supplementary material, Section S10, for evolution of other parameters). The scaling factor A (Fig. 2e) monotonically decays resembling evolution of exciton bleach in open cavities, albeit with different time constants (*e.g.*, due to different photonic environment²⁸). This further supports that significant part of the polaritonic response originates from the dynamics of dark excitons. The exciton bleach dynamics is in turn correlated with the course of SF in which the amount of dark triplet excitons peaks on a sub-100 ps time scale. The dynamics of the Rabi energy V (Fig. 2f) is also strongly correlated with the dynamics of triplet excitons generated via SF. We note that the optical messengers of SF and polaritonic response are energetically far from each other. The observed strong correlation, therefore, indicates that it is possible to enhance sensitivity at a selected spectral range towards physical phenomena that are otherwise more challenging to detect (*e.g.*, due to their weak nature or "inconvenient" energies) by simply tuning cavity resonance to overlap with correlated transitions that are more convenient for detection.

Notably, the phase offsets $\tilde{\phi}_{\pm}$ (Fig. 2g,h) for the two samples evolve in opposite directions and converge to same values for long pump-probe delays where most of the initial excitations are relaxed and the dynamics is mostly governed by the dynamics of triplet excitons. Their

values for UP and LP lay on the opposite sides of the case of pure bleach-like spectrum ($\tilde{\phi}_{\pm} = 90^{\circ}$). Overall, the phase values and the direction of their evolution are in full agreement with the intuitive picture in Fig. 2a, and indicate relaxation of the dispersive response towards a more symmetric lineshape with dominating loss components.

The extracted phases should be considered as "effective", since they reflect combined dynamics in organic and metal films. To gain insights into constitution of the observed gain-loss spectra, we carried out *ab initio* electromagnetic simulations based on TM method,^{56,57} and a statistical correlation analysis of a large pump-probe dataset. In the next section, the mechanism behind solely dark excitons shaping the polaritonic response is considered, followed by the description of effects from metal films.

Dark excitons add opposite phases to UP and LP

To pinpoint the effects of dark excitons, we simulate four fundamental refractive-index changes (Fig. 3a–d) of (i) the amount of excitons available for coupling (bleach), (ii) broadening of exciton lineshape, (iii) refractive-index offset, and (iv) exciton energy shift (see Supplementary material, Section S12). The choice of altering the refractive index (and not the extinction coefficient) is justified by its direct relation to the real part of pump-induced phase $\delta\phi(E) = \Re\left((\Delta n(E) + i\Delta\kappa(E))Ed/(\hbar c)\right)$ where $\Delta n(E) = n_{\text{ON}}(E) - n_{\text{OFF}}(E)$ is the change of the refractive index, and $\Delta\kappa(E) = \kappa_{\text{ON}}(E) - \kappa_{\text{OFF}}(E)$ is the change of the absorption coefficient that is related to $\Delta n(E)$ via Kramers-Kronig relationship;^{58,59} c is the speed of light in vacuum. It is clear that it is only changes in dark-exciton population and spectral broadening that are capable of adding opposite phases to UP and LP (Fig. 3a,b), whereas refractive-index offsets and energy shifts add phases of the same sign (Fig. 3c,d). We note that the change in the refractive-index offset alone would result in the doubly-dispersive profile with the same sign of dispersiveness for both LP and UP, which was observed previously theoretically¹⁶ and experimentally.²⁷ This case is not evident here, indicating that it is rather pump-induced change in bleach and/or spectral broadening that contribute to a

greater extent.

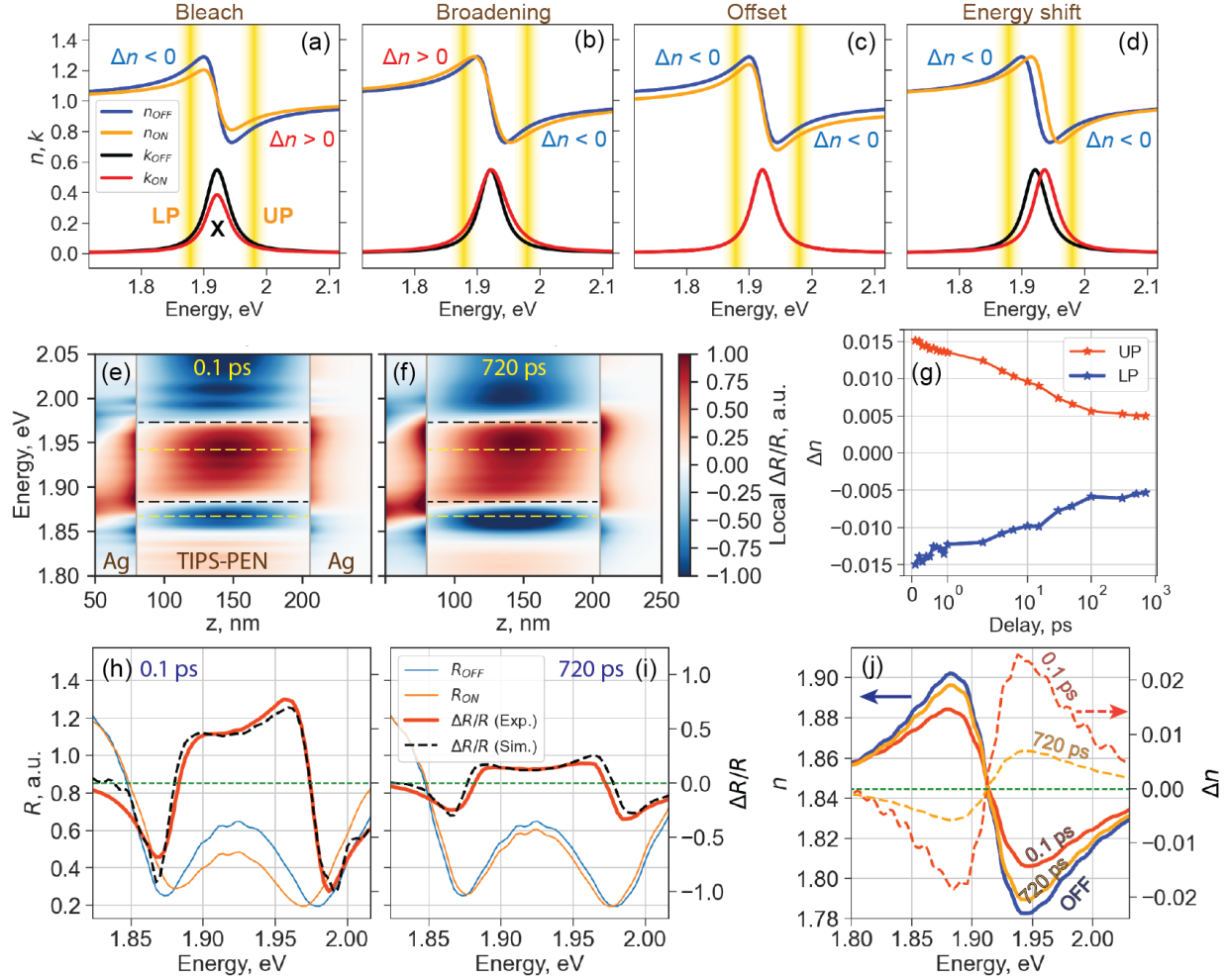


Figure 3: The effects of the dark-excitons' refractive-index (n) change (Δn) for thin cavity ($d = 139$ nm). (a-d) Cartoon summarizing pump-induced changes considered in optical simulations. (a) Scaling by a factor of 1.3 corresponding to the change in bleach of dark excitons; (b) broadening by a factor of 1.3; (c) refractive-index offset by -0.05; (d) energy shift by 15 meV. In the regions of normal dispersion, the signs of the refractive index change are indicated. (e,f) Normalized axially-resolved TM simulations of local $\Delta R/R$ spectra for (e) 0.1 and (f) 720 ps pump-probe delays. Metal (Ag) and organic (TIPS-PEN) layers are indicated. Dashed lines serve as references for convenience of the reader. (g) Time-resolved refractive-index changes of the organic layer at the energies of LP (blue) and UP (red). (h,i) TM fittings of experimental data together with the extracted R_{ON} and R_{OFF} spectra for pump-probe delays of (h) 0.1 ps and (i) 720 ps. (j) Time-resolved dynamics of the refractive index n of TIPS-PEN and its change Δn .

The measured DR spectra were fitted (using NSGA-II algorithm⁶⁰) with simulated spectra for an array of pump-probe delays. The dispersive structures in the retrieved axially-

resolved DR spectra (Fig. 3e,f) are evident at the positions of UP and LP in the organic layer, extending into the metal films in accordance with the Maxwell’s equations. Different optical properties of the metal films result in the local spectra distorted from the ones in the organic layer with the net effect of mild shaping of axially-integrated DR lineshapes shown in Fig. 3h,i. The splitting between UP and LP increases over time (see retrieved R_{ON} spectra) due to more excitons available for coupling to (probe) photons. This effect, referred to as polariton contraction, was observed previously for vibration-polaritons.^{61,62} Although the fitting quality is not as good as that based on Fano formulae and non-Hermitian Hamiltonian, it is still high provided only four fitting parameters (see Supplementary material, Section S12). This is because TM-based description is intrinsically highly constrained by Maxwell’s equations, geometry of the problem, and optical properties of the materials. A poorer fitting quality indicates, as expected, that additional effects such as those originating from metal layers were not taken into account.

Fig. 3g shows the dynamics of the refractive index of the organic layer at the energies of LP and UP (see also Supplementary material, Section S13). As a result of pump excitation, the refractive index experienced by probe-induced LPs became lower, whereas that experienced by UPs increased, with both values relaxing towards unperturbed value at larger pump-probe delays. The change of the organic layer’s refractive index at the beginning and end of the measurement interval (Fig. 3j) qualitatively matches the case of dark-excitons-induced changes shown in Fig. 3a (although broadening also took place). No prominent refractive-index offset was observed in the simulations resulting in discernible dispersive lineshapes of opposite signs at LP and UP energies.

We note that the retrieved refractive-index changes are overestimated since pump-induced optical effects of the metallic layers were not explicitly taken into account: the dynamics in both organic and metal films are embedded into the retrieved behaviour of the organic-layer’s refractive index. Nevertheless, since it was possible to fit reasonably well the measured response at multiple pump-probe delays with parameters related to solely dark excitons, we

therefore conclude that dark excitons play a significant role in shaping polaritonic response. Next, we improve fitting quality of TM simulations by allowing metals to respond dynamically to the pump excitation, and finally identify the contribution from hot electrons using a statistical correlation analysis.

Metal layers contribute absorptive polaritonic response

To account for perturbations in metal mirrors, they were made to respond to the optical excitation as well, with the pump-induced refractive-index changes of the organic layer extracted in the previous section guiding the optimization process. Fig. 4a,b show axially-resolved DR spectra at 0.1 ps and 720 ps. Within the organic layer, the general trend of increasing splitting between the positive peaks with pump-probe delays can be discerned similarly to the sole effect of dark excitons discussed above (Fig. 3e,f). This indicates that dark excitons still contribute, although to a lesser extent, since the effects of metal layers have to be also accommodated. The negative components in this case predominantly originated from metal layers, especially, from partially-transmitting 30-nm silver film ultimately giving rise to differential dispersive response at the energies of polaritonic modes (Fig. 4c,d). This absorptive contribution from metal films is sensible, because metals exhibit orders of magnitude stronger nonlinearities amongst other materials, which are accessible in thin metal films coupled to Lorentz-like oscillators⁴² (polaritons in our case). This is because thin films transmit a small fraction of light due to the final penetration depth of electric field into metals,^{63–65} with the transmitted light carrying information on these nonlinearities. It is arguable that small penetration depth would contribute only small signal to the axially-integrated response. However, small thickness of silver film is offset by its very large absorption coefficient thus enhancing absorptive contribution.

Retrieved reflectance and DR spectra (Fig. 4c,d) are similar to the ones in Fig. 3h,i, but yielding a significantly improved fitting quality comparable to the quality of Fano-formulae- and non-Hermitian-Hamiltonian-based fittings. To check for sensibility of the retrieved re-

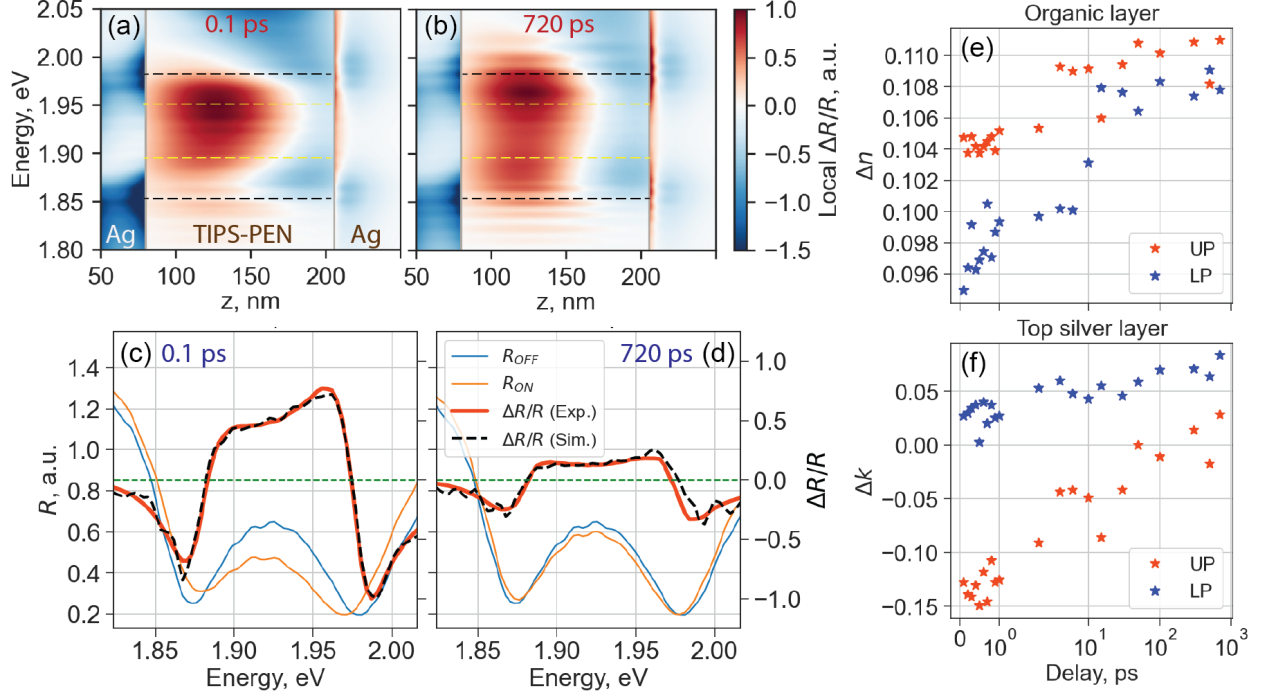


Figure 4: The effects of the metallic response for thin cavity ($d = 139$ nm). (a–d) Normalized axially-resolved TM simulations of (a,b) local and (c,d) integrated $\Delta R/R$ spectra for (a,c) 0.1 and (b,d) 720 ps pump-probe delays. In (a,b), metal (Ag) and organic (TIPS-PEN) layers are indicated. Dashed lines serve as references for convenience of the reader. In (c,d), reflectance spectra R_{ON} and R_{OFF} are also shown. (e,f) Changes of (e) refractive index of the organic layer and (f) extinction coefficient of the thin metal film versus pump-probe delay at the energies of LP (blue) and UP (red).

flectance spectra R_{ON} and R_{OFF} , we experimentally confirmed their behaviour at short and long pump-probe delays using similar cavities (see Supplementary material, Section S14).

It is now possible to qualitatively relate made observations to the phases $\tilde{\phi}_{\pm}$ extracted from non-Hermitian description of polaritonic response. These phases correspond to net quantities containing the response of both metal ($\tilde{\phi}_{Ag,\pm} \sim 90^\circ$) and organic ($\tilde{\phi}_{TIPS-PEN,-} \sim -45^\circ$ and $\tilde{\phi}_{TIPS-PEN,+} \sim -135^\circ$) layers (see Fig. 2a). Metals contribute mostly loss signal whereas organic layer contributes mostly gain signal.

As mentioned, strong polariton delocalization renders polaritons potentially susceptible not only to dark excitons in the organic layer but also to hot electrons in metal films. These electrons are known to evolve in accordance with a two-temperature model:^{27,66} the majority of the dynamics occurs within the first time constant (~ 1 ps, electron-electron scattering) and

the rest of the dynamics occurs within the second time-constant (~ 10 ps, electron-phonon scattering). Fig. 4e,f show pump-induced dynamics of the refractive index (organic layer) and extinction coefficient (metal film) at the energies of UP and LP (other parameters did not show prominent dynamics). Stochastic nature of optimization during TM-based fittings, however, resulted in large noise in the retrieved dynamics (Fig. 4f), making unambiguous determination of the two time-constants challenging. Therefore, to confirm the presence of hot electrons, we performed a more powerful statistical correlation analysis of a large pump-probe dataset, which is described next.

An imprint of hot electrons in the polaritonic response

The large pump-probe dataset was additionally measured in a large variety of experimental conditions (Table 2) with the overall number of statistical samples equal to 150 (72 measurements on open cavities and 78 measurements on closed cavities). Each of the data-samples was split into two parts in energy-domain (Fig. 5a): a high-energy part containing weak optical response from singlet and triplet excitons (*i.e.*, excitonic response) and a lower-energy part containing strong polaritonic response. From each of these parts, time-constants were extracted via the global analysis of pump-probe spectra^{28,67} and correlated between excitonic and polaritonic responses separately for open and closed cavities (Fig. 5b). Measurements on open optical microcavities served as a statistical reference.

Table 2: Experimental parameters and their value-ranges for statistical correlation analysis of measured data.

| Parameter | Range of values |
|--------------|---------------------------------|
| Cavity type | open, closed |
| Pump energy | X_α , X_β , LP, UP |
| Pump fluence | 5–66 nJ |
| Cavity mode | 1.71–1.98 eV |

In the case of open cavities, as expected, average time constants (yellow markers) laid predominantly on the diagonal since both lower- and higher-energy responses corresponded

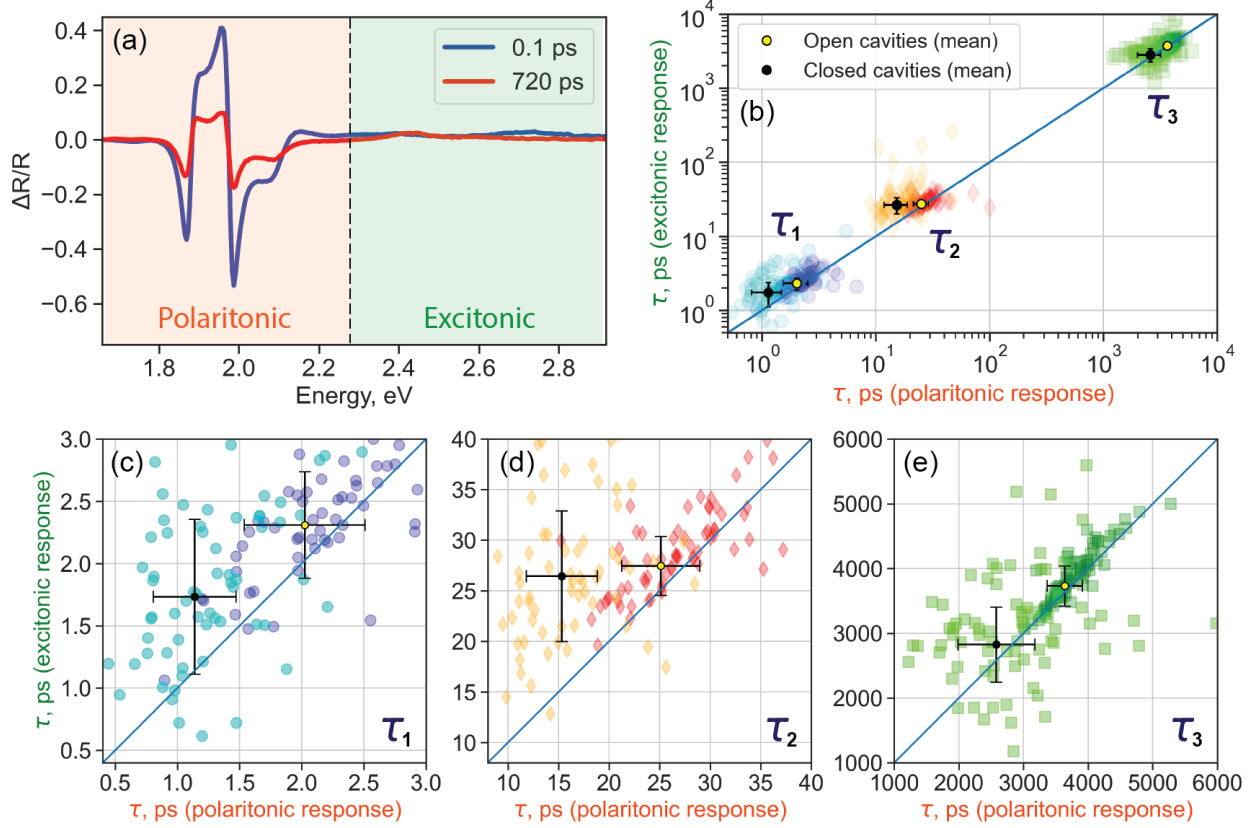


Figure 5: Signatures of hot electrons. (a) Separation of transient spectra into polaritonic (shaded orange) and molecular (shaded green) response. (b–e) Correlation of time-constants extracted from molecular and polaritonic responses.

to the dynamics of singlet and triplet excitons, and no polaritonic effects were at play. In the case of closed cavities, all three time constants (black markers) became shorter with the first two significantly deviating from the diagonal. We note that shorter time-constants in the closed cavities can result from the two effects: (i) Purcell effect²⁸ (which on its own would yield time-constants $\tau_{Purcell,i}$ $i = 1, 2, 3$), and (ii) hot electrons in silver films relaxing in accordance with a two-temperature model (with time-constants $\tau_{Ag,i}$ $i = 1, 2$). The contribution of the latter effect to shortening of the time-constants is indeed possible since the first two time-constants (τ_i , $i = 1, 2$) measured in experiments are of the same order of magnitude as typical time-constants describing the dynamics of hot electrons in metals ($\tau_{Ag,1} \sim 1$ ps, $\tau_{Ag,2} \sim 10$ ps). Therefore the measured time-constants τ_i ($i = 1, 2$) reflect net values such that $\min(\tau_{Ag,i}, \tau_{Purcell,i}) < \tau_i < \max(\tau_{Ag,i}, \tau_{Purcell,i})$ (see Supplementary material,

Section S15, for more details). The two effects, however, are possible to disentangle since the Purcell effect is characterized by time-independent local density of photonic states but not the real number of photons in the cavity, and therefore shortening of the three time-constants should be by a similar (if not the same) factor, whereas the effect of hot electrons is time-dependent. Indeed, Fig. 5c–e show that the three time-constants are displaced horizontally by different amounts, with the first two being displaced to a greater extent than the third time-constant confirming contribution from hot electrons. Provided all insights gained so far, the observed differences in the loss signal before 10 ps pump-probe delay for thin and thick cavities (Figure 1e,f) are attributed to the dynamics of hot electrons in different photonic environments modulating absorptive response in the metal films.

Discussion

In summary, we investigated the polaritonic response from low-Q organic optical microcavities with TIPS-PEN and silver layers using steady-state and ultrafast-spectroscopy experiments. Non-Hermitian description of the detected gain-loss spectra allowed us to conclude that the dynamics of the Rabi splitting was strongly correlated with the fission of dark singlet excitons in the organic layer. In addition, polaritons delocalized over both organic and metal films were found to carry information on hot electrons evolving in accordance with a two-temperature model. These contributions resulted in doubly-dispersive Fano-like spectra formed as a result of intricate interplay between metal and organic films.

In this work, we identified that dark excitons add opposite phases to the two polaritonic branches. It is worth noting that the relaxation of hot electrons could add additional transient phase offsets between R_{ON} and R_{OFF} signals through the changing penetration depth of metal mirrors.⁶⁸ This could affect the cavity optical length and position of the cavity mode as well as its bandwidth.⁶³ In this case, the two mirrors would also generally contribute different phase offsets. Thus, for example, for an unperturbed case, the phase shift upon reflection

from a 30-nm silver film at ~ 1.91 eV was estimated previously to be $\sim 140^\circ$, while for a 100-nm mirror the phase change was higher and similar to that of bulk.⁶⁵ It is not straightforward to disentangle and quantify all phase contributions to polaritonic response at this stage. Further investigations are needed.

The approach outlined in this study holds promise for endeavors to distinguish the pure polaritonic response from excitations in metal layers and subtle dark excitons in the active layer of low-Q optical microcavities. Our research outcomes carry significance for both the exploration and practical applications of manipulating photophysical and photochemical processes using photonics paving the way towards improved designs for optical organic microcavities to enhance control over these processes. This in turn is vital for the potential utilization of microcavities for various applications including energy-efficient organic-based photovoltaics. A more specific application is envisioned based on the observation that, due to small pump-induced changes to the Rabi energy, the response at long sub-ns pump-probe delays corresponds to the mathematical operation of differentiation of polaritonic spectra. This could be viewed as an alternative to analogue differentiation performed using ultrashort optical pulses, which could ultimately be exploited, *e.g.*, in polariton-based spatial light modulators⁶ for spectral differentiation of input beams as part of derivative-based analyses.^{69,70}

Methods

Sample preparation

Fabry-Pérot cavities (Fig. 1c) were prepared on glass substrates (AF32eco, Schott, 25x20x0.5 mm³) cleaned by sonication (10 minutes) in alkaline solution (Hellmanex), deionized water and 2-propanol. 100-nm silver films were deposited by thermal evaporation. TIPS-PEN (6,13-Bis(triisopropylsilylethynyl)pentacene, Ossila Ltd.) and polystyrene (PS, Mw ca. 222k, Polymer Source Inc.) were used as received. In manufacturing the active layer, PS was dissolved in toluene at a concentration of 20 mg.mL⁻¹, and TIPS-PEN was added to the

solution with relative mass ratio of 30%. Thin films of TIPS-PEN/PS were prepared by spincoating and their thicknesses were adjusted with the spin rate (1800 and 2000 rpm for the thick and thin sample, respectively). The organic layer thicknesses of thin and thick cavities are 139 nm and 148 nm, respectively. The thin films were then annealed for 1 minute at 100°C to remove traces of residual solvent. Then, 30 nm silver films were thermally evaporated on top. Finally, 50 nm protective layer of aluminium oxide (AlO_x) were deposited on top of the cavities via atomic layer deposition (Ultratech, Savannah S100, precursor trimethyl-aluminium, Strem Chemicals, Inc.) at 80°C.

Angle-resolved steady-state reflectance spectroscopy

Absorption spectrum of TIPS-PEN/PS thin film was acquired with an Agilent Cary 6000i UV-Vis-NIR absorption spectrometer. Angle-resolved steady-state reflectance spectra of the Fabry-Pérot cavities (Fig. 1a-b) were acquired in a home-built Fourier microscopy setup⁷¹ using a halogen light source (Ocean Optics, HL-2000-HP) focused onto the sample via an objective (60x, NA=0.9, Olympus, MPLAPON60X). The reflected light was imaged from the back focal plane of the objective onto the entrance slit of a spectrometer (Princeton Instruments IsoPlane SCT 320). A linear polarizer was used to select TE polarization. The resulting spectra were acquired with a Si-CCD camera (Princeton Instruments, PIXIS:400).

Transient reflectance spectroscopy

Transient reflectance spectroscopy (shown schematically in Fig. 1c) performed in this work is described elsewhere.²⁸ In a nutshell, an amplified Ti:Sapphire oscillator (Coherent Libra) produced 80 fs 1.55 eV optical pulses at 1 kHz. These in turn were split to drive a lab-built noncollinear optical parametric amplifier generating pump pulses (39 fs, 1.91 eV, 20 nJ, p-polarized), and CaF_2 white-light generator generating p-polarized probe pulses covering

1.65–2.88 eV. Differential reflectance

$$\frac{\Delta R}{R} = -\frac{R_{\text{ON}}(E, \tau) - R_{\text{OFF}}(E)}{R_{\text{OFF}}(E)} \quad (7)$$

was acquired, where R_{OFF} is reflectance of the probe beam from unperturbed sample, R_{ON} is that from the pumped sample, τ is pump-probe delay, E is detection energy. The resolution of the experiment was 100 fs.

References

1. Lee, A. J.; Spence, D. J.; Pask, H. M. Terahertz sources based on stimulated polariton scattering. *Progress in Quantum Electronics* **2020**, *71*, 100254.
2. Deng, H.; Weihs, G.; Snoke, D.; Bloch, J.; Yamamoto, Y. Polariton lasing vs. photon lasing in a semiconductor microcavity. *Proceedings of the National Academy of Sciences* **2003**, *100*, 15318–15323.
3. Ballarini, D.; Giorgi, M. D.; Cancellieri, E.; Houdré, R.; Giacobino, E.; Cingolani, R.; Bramati, A.; Gigli, G.; Sanvitto, D. All-optical polariton transistor. *Nature Communications* **2013**, *4*, 1778.
4. Xu, Y.; Wu, L.; Ang, L. Surface Exciton Polaritons: A Promising Mechanism for Refractive-Index Sensing. *Physical Review Applied* **2019**, *12*, 024029.
5. Nikolis, V. C.; Mischok, A.; Siegmund, B.; Kublitski, J.; Jia, X.; Benduhn, J.; Hörmann, U.; Neher, D.; Gather, M. C.; Spoltore, D.; Vandewal, K. Strong light-matter coupling for reduced photon energy losses in organic photovoltaics. *Nature Communications* **2019**, *10*, 3706.
6. Jing-Quan, W.; Peng, H.; Jing-Lei, D.; Yong-Kang, G.; Xian-Gang, L.; Chun-Lei, D.

- Spatial Light Modulator Based on Surface Plasmon Polaritons for Chromatic Display. *Chinese Physics Letters* **2008**, *25*, 2908–2911.
7. Ghosh, S.; Liew, T. C. H. Quantum computing with exciton-polariton condensates. *npj Quantum Information* **2020**, *6*, 16.
 8. Kasprzak, J.; Richard, M.; Kundermann, S.; Baas, A.; Jeambrun, P.; Keeling, J. M. J.; Marchetti, F. M.; Szymańska, M. H.; André, R.; Staehli, J. L.; Savona, V.; Littlewood, P. B.; Deveaud, B.; Dang, L. S. Bose–Einstein condensation of exciton polaritons. *Nature* **2006**, *443*, 409–414.
 9. Amo, A.; Lefrère, J.; Pigeon, S.; Adrados, C.; Ciuti, C.; Carusotto, I.; Houdré, R.; Giacobino, E.; Bramati, A. Superfluidity of polaritons in semiconductor microcavities. *Nature Physics* **2009**, *5*, 805–810.
 10. Nguyen, H.; Gerace, D.; Carusotto, I.; Sanvitto, D.; Galopin, E.; Lemaître, A.; Sagnes, I.; Bloch, J.; Amo, A. Acoustic Black Hole in a Stationary Hydrodynamic Flow of Microcavity Polaritons. *Physical Review Letters* **2015**, *114*, 036402.
 11. Hobson, P. A.; Barnes, W. L.; Lidzey, D. G.; Gehring, G. A.; Whittaker, D. M.; Skolnick, M. S.; Walker, S. Strong exciton–photon coupling in a low-Q all-metal mirror microcavity. *Applied Physics Letters* **2002**, *81*, 3519–3521.
 12. Pradeesh, K.; Baumberg, J. J.; Prakash, G. V. Strong exciton-photon coupling in inorganic-organic multiple quantum wells embedded low-Q microcavity. *Optics Express* **2009**, *17*, 22171.
 13. Schwartz, T.; Hutchison, J. A.; Léonard, J.; Genet, C.; Haacke, S.; Ebbesen, T. W. Polariton Dynamics under Strong Light–Molecule Coupling. *ChemPhysChem* **2012**, *14*, 125–131.

14. Zhong, X.; Chervy, T.; Wang, S.; George, J.; Thomas, A.; Hutchison, J. A.; Devaux, E.; Genet, C.; Ebbesen, T. W. Non-Radiative Energy Transfer Mediated by Hybrid Light-Matter States. *Angewandte Chemie International Edition* **2016**, *55*, 6202–6206.
15. DelPo, C. A.; Kudisch, B.; Park, K. H.; Khan, S.-U.-Z.; Fassioli, F.; Fausti, D.; Rand, B. P.; Scholes, G. D. Polariton Transitions in Femtosecond Transient Absorption Studies of Ultrastrong Light–Molecule Coupling. *The Journal of Physical Chemistry Letters* **2020**, *11*, 2667–2674.
16. Renken, S.; Pandya, R.; Georgiou, K.; Jayaprakash, R.; Gai, L.; Shen, Z.; Lidzey, D. G.; Rao, A.; Musser, A. J. Untargeted effects in organic exciton–polariton transient spectroscopy: A cautionary tale. *The Journal of Chemical Physics* **2021**, *155*, 154701.
17. Hirai, K.; Hutchison, J. A.; Uji-i, H. Molecular Chemistry in Cavity Strong Coupling. *Chemical Reviews* **2023**, *123*, 8099–8126.
18. Quach, J. Q.; McGhee, K. E.; Ganzer, L.; Rouse, D. M.; Lovett, B. W.; Gauger, E. M.; Keeling, J.; Cerullo, G.; Lidzey, D. G.; Virgili, T. Superabsorption in an organic micro-cavity: Toward a quantum battery. *Science Advances* **2022**, *8*, eabk3160.
19. Ballarini, D.; Giorgi, M. D.; Gambino, S.; Lerario, G.; Mazzeo, M.; Genco, A.; Accorsi, G.; Giansante, C.; Colella, S.; D'Agostino, S.; Cazzato, P.; Sanvitto, D.; Gigli, G. Polariton-Induced Enhanced Emission from an Organic Dye under the Strong Coupling Regime. *Advanced Optical Materials* **2014**, *2*, 1076–1081.
20. Wang, M.; Hertzog, M.; Börjesson, K. Polariton-assisted excitation energy channeling in organic heterojunctions. *Nature Communications* **2021**, *12*, 1874.
21. Martínez-Martínez, L. A.; Du, M.; Ribeiro, R. F.; Kéna-Cohen, S.; Yuen-Zhou, J. Polariton-Assisted Singlet Fission in Acene Aggregates. *The Journal of Physical Chemistry Letters* **2018**, *9*, 1951–1957.

22. Polak, D.; Jayaprakash, R.; Lyons, T. P.; Martínez-Martínez, L. Á.; Leventis, A.; Fallon, K. J.; Coulthard, H.; Bossanyi, D. G.; Georgiou, K.; Anthony J. Petty, I.; Anthony, J.; Bronstein, H.; Yuen-Zhou, J.; Tartakovskii, A. I.; Clark, J.; Musser, A. J. Manipulating molecules with strong coupling: harvesting triplet excitons in organic exciton microcavities. *Chemical Science* **2020**, *11*, 343–354.
23. Du, M.; Martínez-Martínez, L. A.; Ribeiro, R. F.; Hu, Z.; Menon, V. M.; Yuen-Zhou, J. Theory for polariton-assisted remote energy transfer. *Chemical Science* **2018**, *9*, 6659–6669.
24. Liu, B.; Menon, V. M.; Sfeir, M. Y. The Role of Long-Lived Excitons in the Dynamics of Strongly Coupled Molecular Polaritons. *ACS Photonics* **2020**, *7*, 2292–2301.
25. Gu, B.; Mukamel, S. Optical-Cavity Manipulation of Conical Intersections and Singlet Fission in Pentacene Dimers. *The Journal of Physical Chemistry Letters* **2021**, *12*, 2052–2056.
26. Climent, C.; Casanova, D.; Feist, J.; Garcia-Vidal, F. J. Not dark yet for strong light-matter coupling to accelerate singlet fission dynamics. *Cell Reports Physical Science* **2022**, *3*, 100841.
27. Liu, B.; Menon, V. M.; Sfeir, M. Y. Ultrafast thermal modification of strong coupling in an organic microcavity. *APL Photonics* **2021**, *6*, 016103.
28. Kolesnichenko, P. V.; Hertzog, M.; Hainer, F.; Deschler, F.; Zaumseil, J.; Buckup, T. *submitted* **2024**, *128*, 1496–1504.
29. Takahashi, S.; Watanabe, K.; Matsumoto, Y. Singlet fission of amorphous rubrene modulated by polariton formation. *The Journal of Chemical Physics* **2019**, *151*, 074703.
30. Xiang, B.; Ribeiro, R. F.; Li, Y.; Dunkelberger, A. D.; Simpkins, B. B.; Yuen-Zhou, J.;

- Xiong, W. Manipulating optical nonlinearities of molecular polaritons by delocalization. *Science Advances* **2019**, *5*, eaax5196.
31. Fano, U. Effects of Configuration Interaction on Intensities and Phase Shifts. *Physical Review* **1961**, *124*, 1866–1878.
 32. Limonov, M. F.; Rybin, M. V.; Poddubny, A. N.; Kivshar, Y. S. Fano resonances in photonics. *Nature Photonics* **2017**, *11*, 543–554.
 33. Caselli, N.; Intonti, F.; China, F. L.; Biccari, F.; Riboli, F.; Gerardino, A.; Li, L.; Linfield, E. H.; Pagliano, F.; Fiore, A.; Gurioli, M. Generalized Fano lineshapes reveal exceptional points in photonic molecules. *Nature Communications* **2018**, *9*, 396.
 34. Lin, M.-F.; Pfeiffer, A. N.; Neumark, D. M.; Leone, S. R.; Gessner, O. Strong-field induced XUV transmission and multiplet splitting in $4d^{-1}6p$ core-excited Xe studied by femtosecond XUV transient absorption spectroscopy. *The Journal of Chemical Physics* **2012**, *137*, 244305.
 35. Liao, C.-T.; Sandhu, A. XUV Transient Absorption Spectroscopy: Probing Laser-Perturbed Dipole Polarization in Single Atom, Macroscopic, and Molecular Regimes. *Photonics* **2017**, *4*, 17.
 36. Levi, F.; Camparo, J.; Francois, B.; Calosso, C. E.; Micalizio, S.; Godone, A. Precision test of the ac Stark shift in a rubidium atomic vapor. *Physical Review A* **2016**, *93*, 023433.
 37. Barontini, G.; Blackburn, L.; Boyer, V.; Butuc-Mayer, F.; Calmet, X.; López-Urrutia, J. R. C.; Curtis, E. A.; Darquié, B.; Dunningham, J.; Fitch, N. J.; Forgan, E. M.; Georgiou, K.; Gill, P.; Godun, R. M.; Goldwin, J.; Guarrera, V.; Harwood, A. C.; Hill, I. R.; Hendricks, R. J.; Jeong, M. *et al.* Measuring the stability of fundamental constants with a network of clocks. *EPJ Quantum Technology* **2022**, *9*, 12.

38. Salikhov, K. M. Consistent Paradigm of the Spectra Decomposition into Independent Resonance Lines. *Applied Magnetic Resonance* **2016**, *47*, 1207–1227.
39. Mun, S.-E.; Yun, H.; Choi, C.; Kim, S.-J.; Lee, B. Enhancement and Switching of Fano Resonance in Metamaterial. *Advanced Optical Materials* **2018**, *6*, 1800545.
40. Qi, J.; Chen, Z.; Chen, J.; Li, Y.; Qiang, W.; Xu, J.; Sun, Q. Independently tunable double Fano resonances in asymmetric MIM waveguide structure. *Optics Express* **2014**, *22*, 14688.
41. Zhang, T.; Zhang, D.; Zhang, H.-F. Realization of double Fano resonances with a InSb-doped Fabry-Perot cavity. *Results in Physics* **2022**, *35*, 105417.
42. Owens, D. T.; Fuentes-Hernandez, C.; Hales, J. M.; Perry, J. W.; Kippelen, B. Nonlinear optical properties of induced transmission filters. *Optics Express* **2010**, *18*, 19101.
43. Moiseyev, N.; Certain, P.; Weinhold, F. Resonance properties of complex-rotated hamiltonians. *Molecular Physics* **1978**, *36*, 1613–1630.
44. Kukulin, V. I.; Krasnopol'sky, V. M.; Horáček, J. *Theory of Resonances*; Springer Netherlands, 1989.
45. Durand, P.; Paidarová, I.; Gadéa, F. X. Theory of Fano profiles. *Journal of Physics B: Atomic, Molecular and Optical Physics* **2001**, *34*, 1953–1966.
46. Paidarová, I.; Durand, P. Quantum Resonances: Line Profiles and Dynamics. *Collection of Czechoslovak Chemical Communications* **2003**, *68*, 529–553.
47. Heiss, W.; Harney, H. The chirality of exceptional points. *The European Physical Journal D* **2001**, *17*, 149–151.
48. Hodaei, H.; Hassan, A. U.; Wittek, S.; Garcia-Gracia, H.; El-Ganainy, R.; Christodoulides, D. N.; Khajavikhan, M. Enhanced sensitivity at higher-order exceptional points. *Nature* **2017**, *548*, 187–191.

49. Wen, J.; Jiang, X.; Jiang, L.; Xiao, M. Parity-time symmetry in optical microcavity systems. *Journal of Physics B: Atomic, Molecular and Optical Physics* **2018**, *51*, 222001.
50. Öztürk, F. E.; Lappe, T.; Hellmann, G.; Schmitt, J.; Klaers, J.; Vewinger, F.; Kroha, J.; Weitz, M. Observation of a non-Hermitian phase transition in an optical quantum gas. *Science* **2021**, *372*, 88–91.
51. Wang, C.; Sweeney, W. R.; Stone, A. D.; Yang, L. Coherent perfect absorption at an exceptional point. *Science* **2021**, *373*, 1261–1265.
52. Dietz, B.; Friedrich, T.; Metz, J.; Miski-Oglu, M.; Richter, A.; Schäfer, F.; Stafford, C. A. Rabi oscillations at exceptional points in microwave billiards. *Physical Review E* **2007**, *75*, 027201.
53. Heiss, W. D. Time behaviour near to spectral singularities. *The European Physical Journal D* **2010**, *60*, 257–261.
54. Tolmachev, A. V.; Masselon, C. D.; Anderson, G. A.; Udseth, H. R.; Smith, R. D. Frequency shifts due to the interference of resolved peaks in magnitude-mode Fourier-transform ion cyclotron resonance mass spectra. *Journal of the American Society for Mass Spectrometry* **2002**, *13*, 387–401.
55. Ott, C.; Kaldun, A.; Raith, P.; Meyer, K.; Laux, M.; Evers, J.; Keitel, C. H.; Greene, C. H.; Pfeifer, T. Lorentz Meets Fano in Spectral Line Shapes: A Universal Phase and Its Laser Control. *Science* **2013**, *340*, 716–720.
56. Pettersson, L. A. A.; Roman, L. S.; Inganäs, O. Modeling photocurrent action spectra of photovoltaic devices based on organic thin films. *J. Appl. Phys.* **1999**, *86*, 487–496.
57. Hecht, E. *Optics, Global Edition*; Pearson, 2016.
58. de L. Kronig, R. On the Theory of Dispersion of X-Rays. *Journal of the Optical Society of America* **1926**, *12*, 547.

59. Toll, J. S. Causality and the Dispersion Relation: Logical Foundations. *Physical Review* **1956**, *104*, 1760–1770.
60. Deb, K.; Pratap, A.; Agarwal, S.; Meyarivan, T. A fast and elitist multiobjective genetic algorithm: NSGA-II. *IEEE Transactions on Evolutionary Computation* **2002**, *6*, 182–197.
61. Dunkelberger, A. D.; Davidson, R. B.; Ahn, W.; Simpkins, B. S.; Owrutsky, J. C. Ultrafast Transmission Modulation and Recovery via Vibrational Strong Coupling. *The Journal of Physical Chemistry A* **2018**, *122*, 965–971.
62. Xiang, B.; Ribeiro, R. F.; Chen, L.; Wang, J.; Du, M.; Yuen-Zhou, J.; Xiong, W. State-Selective Polariton to Dark State Relaxation Dynamics. *The Journal of Physical Chemistry A* **2019**, *123*, 5918–5927.
63. Becker, H.; Burns, S. E.; Tessler, N.; Friend, R. H. Role of optical properties of metallic mirrors in microcavity structures. *Journal of Applied Physics* **1997**, *81*, 2825–2829.
64. Black, C.; Welser, J. Electric-field penetration into metals: consequences for high-dielectric-constant capacitors. *IEEE Transactions on Electron Devices* **1999**, *46*, 776–780.
65. Ma, F.; Liu, X. Phase shift and penetration depth of metal mirrors in a microcavity structure. *Applied Optics* **2007**, *46*, 6247.
66. Temnov, V. V.; Nelson, K. A.; Armelles, G.; Cebollada, A.; Thomay, T.; Leitenstorfer, A.; Bratschitsch, R. Femtosecond surface plasmon interferometry. *Optics Express* **2009**, *17*, 8423.
67. van Stokkum, I. H.; Larsen, D. S.; van Grondelle, R. Global and target analysis of time-resolved spectra. *Biochimica et Biophysica Acta (BBA) - Bioenergetics* **2004**, *1657*, 82–104.

68. Metzner, D.; Olbrich, M.; Lickschat, P.; Horn, A.; Weißmantel, S. Experimental and Theoretical Determination of the Effective Penetration Depth of Ultrafast Laser Radiation in Stainless Steel. *Lasers in Manufacturing and Materials Processing* **2020**, *7*, 478–495.
69. Zangeneh-Nejad, F.; Sounas, D. L.; Alù, A.; Fleury, R. Analogue computing with metamaterials. *Nature Reviews Materials* **2020**, *6*, 207–225.
70. Dubrovkin, J. *Derivative spectroscopy*; Cambridge Scholars Publishing, 2021.
71. Graf, A.; Tropf, L.; Zakharko, Y.; Zaumseil, J.; Gather, M. C. Near-infrared exciton-polaritons in strongly coupled single-walled carbon nanotube microcavities. *Nature Communications* **2016**, *7*, 13078.

Acknowledgements

This research was funded by the Deutsche Forschungsgemeinschaft (DFG) via the Sonderforschungsbereich SFB 1249-B04 and SFB 1249-C09.

Author contributions

M.H. and J.Z. provided samples; P.V.K. conducted the experiments, analyzed and interpreted results; F.H. assisted with data analysis; P.V.K., M.H., O.K. and T.B. participated in discussions; P.V.K. and T.B. wrote the manuscript; P.V.K., M.H. and T.B. revised the manuscript; T.B. secured funding.

Authors disclosure statement

The authors declare no competing interests.

Figure captions

Figure 1. Steady-state and transient spectra of microcavities. (a,b) Normalized angle-resolved steady-state reflectance spectra of (a) thin cavity ($d = 139$ nm) and (b) thick cavity ($d = 148$ nm), with the upper and lower polaritons (UP and LP), dark excitons (X_α and X_β), and cavity mode (C) indicated. Dashed lines represent uncoupled excitonic (horizontal lines) and photonic (parabola) states; solid yellow lines represent hybridized uncoupled (polaritonic) states. (c) Schematics of the transient reflectance experiment. (d) Steady-state absorption spectra of thin (green) and thick (red) cavity, bare TIPS-PEN (dashed and shaded in grey), and pump spectrum (shaded in yellow). (e,f) Transient reflectance spectra at short (0.1 ps, blue) and long (720 ps, red) pump-probe delays of (e) thin and (f) thick cavity. The weak molecular response (dashed) is scaled by a factor of 15 and vertically offset for clarity.

Figure 2. Non-Hermitian Hamiltonian description of transient reflectance spectra. (a) A cartoon explaining the physical meaning of the dynamic phases ϕ_\pm after remapping them onto more intuitive values $\tilde{\phi}_\pm = 90^\circ + 2\phi_\pm$ (modulo 180°). (upper row) "Pump-ON" (red) and "pump-OFF" (blue) reflectance spectra. The inset shows the phase $\tilde{\phi}$ and the direction of the offset of the "pump-ON" spectrum relative to the "pump-OFF" spectrum. (b) Fittings (dashed lines) of short- (red) and long-delay (blue) spectra (solid lines) for thin cavity. (c,d) Raw $\Delta R/R$ spectrum (c) and its corresponding fit (d) for thin cavity. (e–h) The scaling amplitude A (e, solid), coupling strengths V (f, solid), and phases $\tilde{\phi}_\pm$ (g,h) retrieved from fittings. In (e) dashed lines represent the absolute value of the bleach signal from the corresponding open cavities (*i.e.*, cavities without 30-nm metal film). In (f) dashed lines represent T_1 ESA signal from thin and thick cavities.

Figure 3. The effects of the dark-excitons' refractive-index (n) change (Δn) for thin cavity ($d = 139$ nm). (a–d) Cartoon summarizing pump-induced changes considered in optical

simulations. (a) Scaling by a factor of 1.3 corresponding to the change in bleach of dark excitons; (b) broadening by a factor of 1.3; (c) refractive-index offset by -0.05; (d) energy shift by 15 meV. In the regions of normal dispersion, the signs of the refractive index change are indicated. (e,f) Normalized axially-resolved TM simulations of local $\Delta R/R$ spectra for (e) 0.1 and (f) 720 ps pump-probe delays. Metal (Ag) and organic (TIPS-PEN) layers are indicated. Dashed lines serve as references for convenience of the reader. (g) Time-resolved refractive-index changes of the organic layer at the energies of LP (blue) and UP (red). (h,i) TM fittings of experimental data together with the extracted R_{ON} and R_{OFF} spectra for pump-probe delays of (h) 0.1 ps and (i) 720 ps. (j) Time-resolved dynamics of the refractive index n of TIPS-PEN and its change Δn .

Figure 4. The effects of the metallic response for thin cavity ($d = 139$ nm). (a–d) Normalized axially-resolved TM simulations of (a,b) local and (c,d) integrated $\Delta R/R$ spectra for (a,c) 0.1 and (b,d) 720 ps pump-probe delays. In (a,b), metal (Ag) and organic (TIPS-PEN) layers are indicated. Dashed lines serve as references for convenience of the reader. In (c,d), reflectance spectra R_{ON} and R_{OFF} are also shown. (e,f) Changes of (e) refractive index of the organic layer and (f) extinction coefficient of the thin metal film versus pump-probe delay at the energies of LP (blue) and UP (red).

Figure 5. Signatures of hot electrons. (a) Separation of transient spectra into polaritonic (shaded orange) and molecular (shaded green) response. (b–e) Correlation of time-constants extracted from molecular and polaritonic responses.

Table captions

Table 1. Excitonic ($\alpha + \beta$) and photonic (γ) contributions to UP and LP of thin and thick cavities, estimated from Hopfield coefficients averaged across the angles from -5° to 5° (see Supplementary material, Section S2).

Table 2. Experimental parameters and their value-ranges for statistical correlation analysis of measured data.

Supporting Information Available

The following file is available as Supplementary material:

Estimation of the organic-layer thickness and refractive index; Hopfield coefficients; Local electric fields; Transient differential reflectance spectra; SVD decomposition of pump-probe spectra; Fano resonances: a phenomenological description of transient polaritonic response; Reduction of 3D Hilbert space to two dimensions; Non-Hermitian Hamiltonian formalism; Non-Hermitian description of transient response; Non-Hermitian description of transient response with added bleach component; Global exponential fitting of the parameters; Lorentz-oscillator model of dielectric function and Kramers-Kronig relationship; Transfer-matrix simulations of transient reflectance; Experimental R_{OFF} and R_{ON} spectra; A comment on statistical correlation analysis of multiple pump-probe data.